

Article

Investigation on Performance of Various Power Control Strategies with Bifilar Coil for Induction Surface Melting Application

Alagarsamy Sureshkumar ¹, Ramachandiran Gunabalan ², Pradeep Vishnuram ¹, Sridhar Ramsamy ¹ and Benedetto Nastasi ^{3,*}

¹ Department of Electrical and Electronics Engineering, SRM Institute of Science and Technology, Chennai 603 203, India; sureshkumarask2@gmail.com (A.S.); pradeep.kannan03@gmail.com (P.V.); sridharr@srmist.edu.in (S.R.)

² School of Electrical Engineering, VIT Chennai, Chennai 600 127, India; gunabalan1979@gmail.com

³ Department of Planning, Design and Technology of Architecture, Sapienza University of Rome, 00196 Rome, Italy

* Correspondence: benedetto.nastasi@outlook.com

Abstract: In recent years, induction heating applications assisted by electronic power control have been very appealing. For melting applications, induction heating is widely used as it seems to be appropriate and provides higher efficiency, zero pollutants, non-contamination of material, etc. in comparison with conventional heating. The conventional variable frequency control scheme is not sufficient for melting applications because of its high switching loss, low efficiency, and lower heat rate. A superlative control technique is required to control the output power smoothly, for a high heating rate with minimum power loss, and to lower the number of components. In this paper, a capacitorless self-resonating bifilar coil is proposed for induction surface melting applications. The performance of the system in terms of modular losses, heat rate, and efficiency is analyzed for various power methods such as pulse duty cycle control, phase shift control, pulse density modulation control, and asymmetric duty cycle control. An experimental validation is performed for the 1 kW prototype, and the heating rate, efficiency, and modular losses are calculated. The control technique is digitally validated using a PIC16F877A microcontroller with 30 kHz switching frequency. The temperature distribution is analyzed using a FLIR thermal imager. Among the tested methods, pulse density modulation-based control provides smooth and varied power control from 0% to 100% with minimum modular losses. The efficiency of the system is 89% at a rated output power and is greater than 85% for pulse density modulation control with a fast heating rate.



Citation: Sureshkumar, A.; Gunabalan, R.; Vishnuram, P.; Ramsamy, S.; Nastasi, B. Investigation on Performance of Various Power Control Strategies with Bifilar Coil for Induction Surface Melting Application. *Energies* **2022**, *15*, 3301. <https://doi.org/10.3390/en15093301>

Academic Editor: Abu-Siada Ahmed

Received: 23 March 2022

Accepted: 27 April 2022

Published: 30 April 2022

Publisher's Note: MDPI stays neutral with regard to jurisdictional claims in published maps and institutional affiliations.



Copyright: © 2022 by the authors. Licensee MDPI, Basel, Switzerland. This article is an open access article distributed under the terms and conditions of the Creative Commons Attribution (CC BY) license (<https://creativecommons.org/licenses/by/4.0/>).

Keywords: asymmetric duty cycle control; bifilar coil; pulse duty cycle control; induction heating; metal melting; phase shift control; pulse density modulation; series resonant inverter; variable frequency control

1. Introduction

Induction heating (IH) is commonly used in residential, industrial, and medical applications because it has features such as being hygienic; using non-contact heating; providing protection; and having higher competence, higher power density, and specific power control characteristics [1]. The electromagnetic induction principle is used to heat the object directly via the eddy current developed on the load due to I^2R loss [2]. The heat depth of penetration of the load depends on the material's skin depth [3] and the magnitude of the heat depends directly on the frequency of the supply. Therefore, for any real-time applications, the selection of an appropriate operating frequency affects the heating capacity. The switching frequency generally varies from 5 kHz to 1000 kHz, with a load handling capacity of 500 kW [4].

In the recent past, high-frequency resonant inverters with minimum switching losses have enticed researchers to study IH applications. The inverter switches are operated either in zero voltage switching (ZVS) or zero current switching (ZCS) with higher power density, higher efficiency, and light weight [5,6]. Based on the arrangement of the resonant capacitor with respect to the IH load, the inverters are termed as either series-resonant or parallel-resonant inverters. The series-resonant inverter with the voltage source inverter offers better overall performance than the parallel-resonant inverter [7]. Generally, a voltage-source full-bridge series-resonant inverter is preferred for medium-power applications, ranging from 1 kW to 5 kW [8].

Single-switch resonant inverters are used in IH systems where the power requirement is less than 2 kW. Shenkman et al. used a single-switch parallel-resonant AC–AC converter for IH applications [9]. High-frequency ac (HFAC) supply was generated with the single switch connected in series with the supply voltage. The source power factor was improved by an LC filter. The variable frequency power control scheme increased the switching losses. This problem was overcome by using a multi-cycle modulation control technique with a fixed frequency [10]. Two bidirectional semi-conductor SiC junction gate field effect transistor devices were used to convert 50 Hz AC to HFAC. Both switches were operated in soft switching mode to reduce the switching losses.

A half-bridge (HB) series-resonant inverter (SRI) is preferred for applications in which the power ratings range from 2 kW to 4 kW. Ahmed et al. developed a boost HB inverter with an LC branch at the source side [11]. This branch reduces the DC and high-frequency components on the input side, resulting in a higher efficiency. An additional LC network increases the system time constant. Forest et al. developed a multi-winding induction coil-fed IH system to handle irregular shapes of the load [12]. In this system, square and rectangular coils were used and power control was carried out by adjusting the inverter switching frequency. Lucia et al. developed a control algorithm for estimating the load parameters under dynamic variations [13]. The inverter switches were operated with a switching frequency from 20 to 100 kHz, and a control scheme was implemented using a field-programmable gate array (FPGA) controller. Load inductance and resistance were measured for various switching frequencies. Lucia et al. developed a multiple coil-based induction cooking system to deliver power to many loads [14]. The output power was controlled using the PDM technique with minimum switching losses. Lucia et al. developed a multi-inverter operated in discontinuous conduction mode for better efficiency during light load conditions [15].

Power control plays an important role in IH systems. For metal melting applications, mainly pulse width modulation (PWM), pulse density modulation (PDM), asymmetric duty cycle control (ADC), phase shift control (PSC), and variable frequency (VF) control are employed to meet the requirements. A simple DC link PWM control using a thyristor-based rectifier with an input inductor and a DC link capacitor were used to regulate the output voltage [16]. The bulky DC link capacitor increases the overall size of the module. In general, the VF control was used to control the output power for a fixed load [17]. However, ZVS is not feasible if the inverter is operated below the resonant frequency. For constant load operation, pulse width modulation is preferred to regulate the output power based on duty cycle control. This results in a smaller range of soft switching [18]. The efficiency of a PSC-fed inverter was found to be high at a duty cycle greater than 90% [19]. In addition, PDM and AVC control techniques provide better soft-switching ranges. PDM achieves greater efficiency, a wide range of set power control, and soft switching among the above control techniques [20].

In wireless power transfer applications, the self-resonating coil is often used, and its preference depends on the dimensions, frequency, and choice of applications [21]. The virtual capacitance of the coil results in either a series or a parallel resonance depending on the coil structure. In parallel resonance, the magnitude of the impedance seen from the source side is higher, which results in less current being drawn from the supply. Thus, the magnetic field stored in the coil reduces, which results in less heat generation. This problem

is overcome by a current source inverter (CSI) [22], but it draws more reactive power on the secondary side of the coil. These issues are mitigated in series resonance-based bifilar coil [23]. Hence, for real-time heating applications, an RLC series resonance-based bifilar coil is preferred [24]. A capacitorless IH system is proposed in [25], with an RLC series resonance-based bifilar coil.

The main purpose of this work is to perform power control with various modulation techniques such as duty cycle control, VF, PDM, AD,C and PSC to enhance the performance of the bifilar coil-based IH system developed in [25]. Additionally, well-suited modulation techniques are needed for IH systems with less switching loss, a wide range of power control, and a fast heat rate. The developed system decreases the number of resonating components, which reduces the total system size, and uses a suitable control technique for smooth variation with less switching losses.

The rest of this paper is organized as follows: Section 2 describes the circuit description of a bifilar coil-based IH system. Various power control strategies are summarized in Section 3. An experimental validation of various control techniques is performed in Section 4. A summary of the discussions on the experimental results is provided in Section 5. The conclusions of this paper are presented in Section 6.

2. Circuit Description

The circuit of a full-bridge series-resonant inverter is shown in Figure 1. The equivalent DC source is represented in the circuit diagram. Four IGBTs (S_1, S_2, S_3, S_4) with anti-parallel diodes are used to convert the pure DC into high-frequency AC (HFAC). The output of the system is connected to a bifilar coil-fed IH load, where the bifilar coil consists of the equivalent resistance (R_{eq}) and inductance (L_{eq}) [26,27].

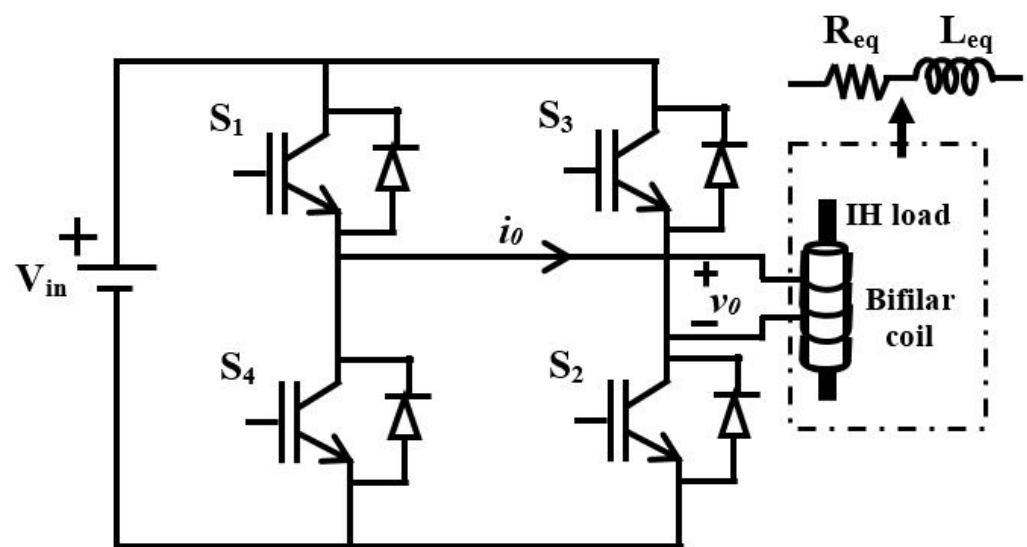


Figure 1. Circuit diagram of a full-bridge series-resonant inverter.

3. Power Control Strategies

In an induction-based melting applications, various temperature profiles are to be considered. As it is required to meet the aforesaid profile, various control techniques are needed to investigate the performance of the system.

3.1. Duty Cycle Control

Duty cycle control is the technique most commonly used to regulate the output power by controlling the duty cycle (D). In this method, the output power is varied by adjusting the on time of the duty cycle. The pulse width is varied in a symmetrical manner in both half cycles to avoid zero sequence components in the output voltage (V_0). During the off period of the IGBTs, the load current freewheels through anti-diodes. Hence, the output

power of the inverter can be varied from 0% to 100% of the rated power by controlling the duty cycle. Typical waveforms of duty cycle control are shown in Figure 2. The resonance condition is not maintained when duty cycle is varied, which results in a lower efficiency. The expression that relates the output power with duty cycle is given by [26]

$$P_0 = \frac{16DV_{in}^2 \cos^2 \Phi}{\pi^2 R_{eq}} \quad (1)$$

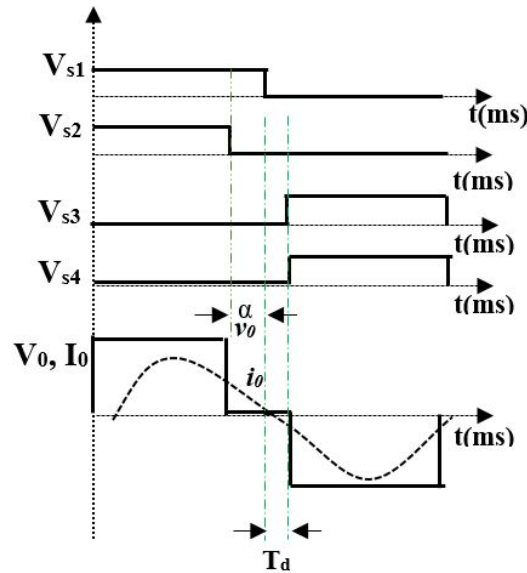


Figure 2. Typical waveforms of duty cycle control.

3.2. Variable Frequency Control

The output power supplied to the work coil can be varied by tuning the switching pulses of the inverter. The frequency of the inverter is decided based on the natural resonance frequency of the resonant tank, which yields maximum output power. If the operating point is moved away from the resonant frequency, the impedance of the system varies, which in turn varies the output power, increases the switching loss, and decreases the efficiency. The output power expression governing the variable frequency is given by [17]

$$P_0 = \frac{1}{1 + \left(\frac{1-f_n}{2\zeta f_n}\right)^2} P_{max} \quad (2)$$

$$\zeta = \frac{R_{eq}}{2} \sqrt{\frac{L_{eq}}{C_r}} \quad (3)$$

where ζ is the damping coefficient and f_n is the normalized switching frequency.

3.3. Phase Shift Control

Typical waveforms of the phase shift control are shown in Figure 3. In this control scheme, the power variation is achieved by shifting the position of the switching pulses between adjacent inverter legs. As the phase angle of switching pulses is shifted from 0° to 180° , the power can be controlled from 0% to 100% of the rated power. The expressions governing the PSC are given by [17]

$$i_0 = \frac{4V_{in}^2 \cos^2\left(\frac{\phi}{2}\right)}{\pi R_{eq}} \quad (4)$$

$$P_0 = \frac{8V_{in}^2 \cos^2(\frac{\phi}{2})}{\pi^2 R_{eq}} \quad (5)$$

For a lower value of ϕ (for 0°), P_0 is maximum as $\cos 0^\circ = 1$, whereas for an increase in ϕ , the output power decreases. In this method, I_0 decreases for an increase in ϕ , which results in a square-shaped source current. This causes a lower input power factor.

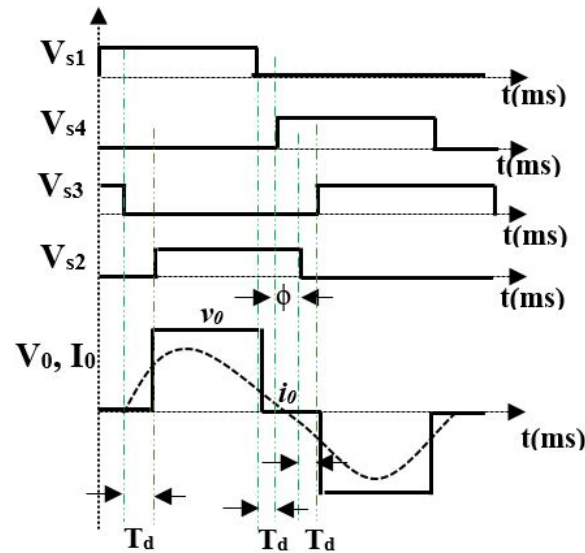


Figure 3. Typical waveforms of phase shift control.

3.4. Asymmetric Duty Cycle Control

For soft switching and power control, asymmetrical duty cycle control is used [28,29]. In this control scheme, the output voltage waveform is made asymmetric, which results in a large dead band for zero crossing of the current. Additionally, the output power is controlled by varying the rms value of the output voltage. Typical waveforms of asymmetric duty cycle control are shown in Figure 4. Because of the asymmetrical voltage waveform, even harmonics will be produced. The expression governing the AVC is given by [29]

$$V_0 = \frac{4V_{in} \cos(\frac{\alpha}{2})}{\pi} \quad (6)$$

$$P_0 = \frac{8V_{in}^2 \cos^2(\frac{\alpha}{2})}{\pi^2 R_{eq}} \quad (7)$$

3.5. Pulse Density Modulation Control

Pulse density modulation is one of the most commonly used techniques for controlling the output power without changing the switching frequency. A constant resonance frequency is maintained throughout the entire switching operation. The density of the switching pulses is varied in order to control the output power by contrasting the high-frequency switching pulses with the low-frequency pulses in compliance with the load specifications. The typical waveforms of pulse density modulation control are shown in Figure 5. The output power expression is given by [30]

$$D_{PDM} = \frac{T_{D,on}}{T_{DPDM}} \quad (8)$$

$$P_0 = D_{PDM} \frac{8V_{in}^2 \cos^2 \Phi}{\pi^2 R_{eq}} \quad (9)$$

where D_{PDM} is the duty cycle of the PDM signal.

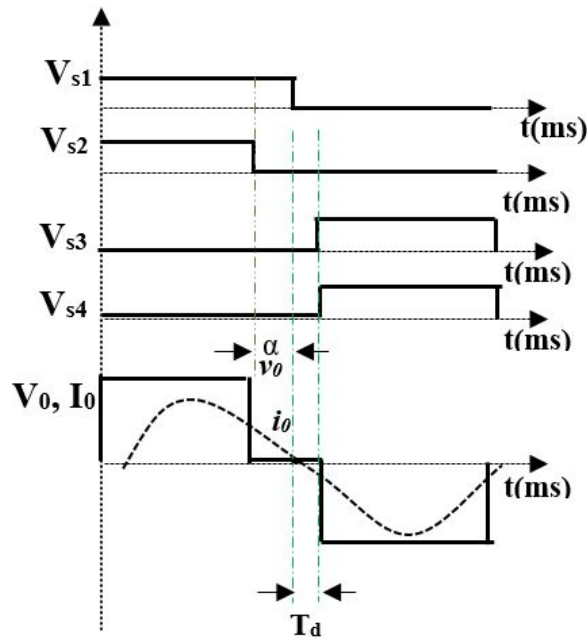


Figure 4. Typical waveforms of asymmetric duty cycle control.

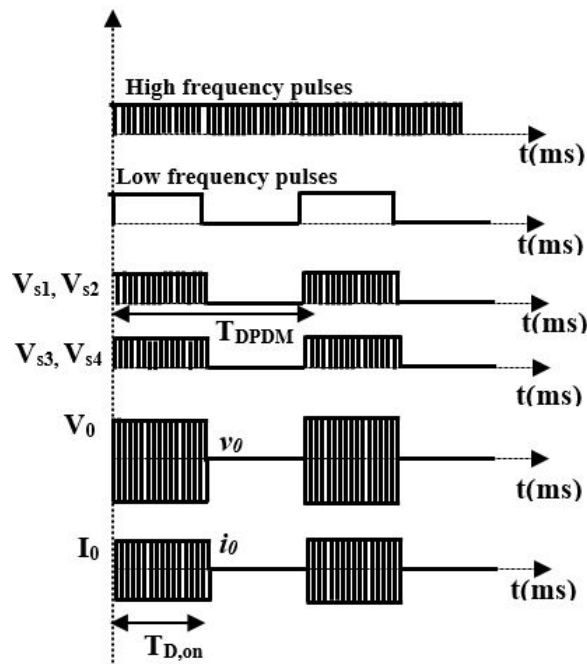


Figure 5. Typical waveforms of pulse density modulation control.

4. Experimental Results

The experimental validation of a bifilar coil-based IH system was performed using an FB inverter with four H20R1203 IGBT power switches. Various control techniques were implemented using PIC16F877A micro controller to obtain HFAC at the load terminal. The TLP250 driver IC amplifies the switching pulses, the SIGLENT CP4060 current probe is used to measure the current, and the digital oscilloscope MDO3024 was used to record the waveform. The advanced FLIR E75 24° thermal imager was used to record the thermal distribution of the load.

The work coil is made with 60 turns of 17 AWG single-layer enamelled-copper wire. The work-piece consists of a metal bar with 25 cm height and 2.5 cm radius. A thermal

insulator was placed between the work coil and the work-piece. The design specifications are listed in Table 1. Figure 6 illustrates the experimental setup for the bifilar coil-based IH system. The experiment was performed to analyze the performance of the IH system in terms of efficiency, power control, and heat transfer rate (16.5 °C/min) for various control techniques.

Table 1. Specifications of the bifilar coil configuration.

Parameters	Values
V_{in}	80 V
L_{eq}	0.02 mH
R_{eq}	10 Ω
f_r	29.5 kHz
f_{sw}	30 kHz
P_{max}	1000 W

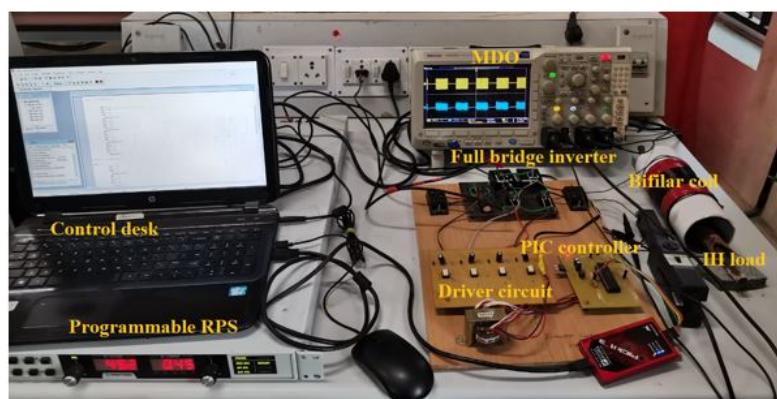
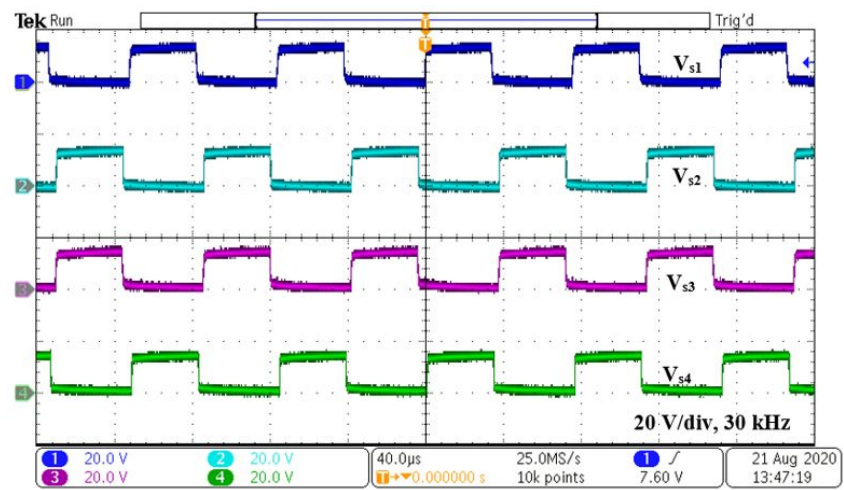


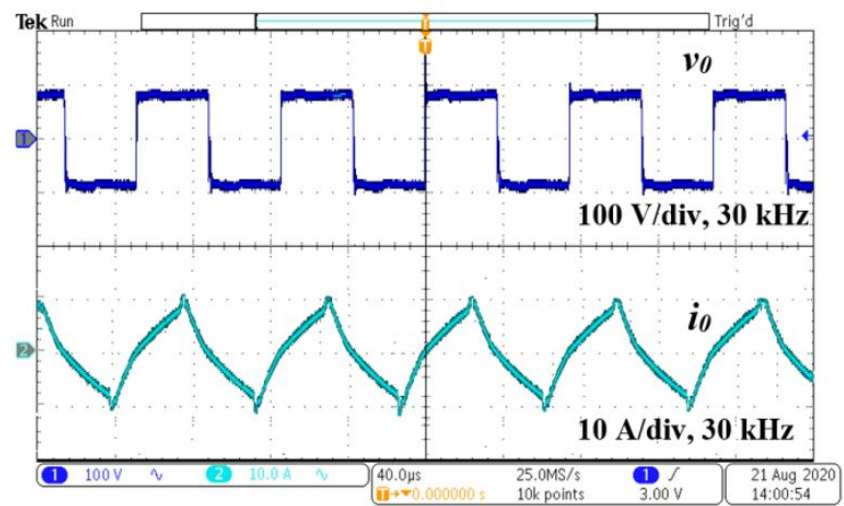
Figure 6. Test setup of the bifilar coil-based IH system.

4.1. Pulse Duty Cycle Control

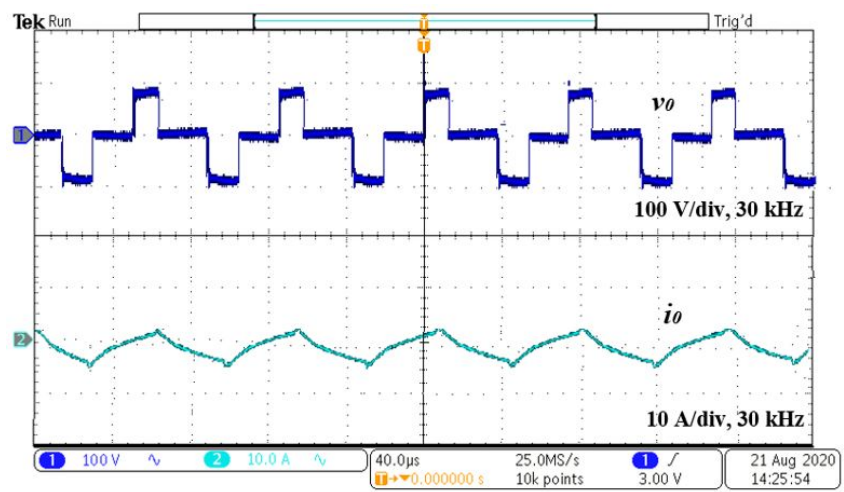
The experimental results of the IH system with pulse duty cycle control are shown in Figure 7. The switching pulses and output voltage (V_0) and current (I_0) waveforms for 50% pulse duty cycle are shown in Figure 7a,b, respectively. The output voltage and current waveforms for 10% pulse duty cycle is shown in Figure 7c. The pulse width variation reduces V_0 and I_0 . At 50% pulse duty cycle and 30 kHz switching frequency, the rms value of the output voltage is 70.71 V and the current is 7.07 A. The output power P_0 is $7.07^2 \times 10 = 500$ W for 10 Ω equivalent resistance. The input power is calculated as $P_{in} = V_{in(dc)} * I_{avg(dc)} = 80 \times 6.97 = 558$ W. The efficiency for 500 W is 89.6%, and for other pulse duty cycle, it is given in Table 2. As it draws more current from the supply, for lower values of duty cycle, the efficiency of the system decreases. The switch (S_1) voltage and current waveforms for 50% pulse duty cycle are shown in Figure 7d. It is inferred that soft switching exists during the on and off periods, which reduces the switching losses. The variation in the temperature with respect to time for 500 W output power is illustrated in Figure 7e. A temperature rise is noted for various duty cycle with the time interval of 5 min, and the heat rate is calculated. The heat rate for various duty cycles is shown in Figure 7f. It is noted that the heat increases and attains 82.5 °C at 50% duty cycle for a period of 5 min. The thermal image for various pulse duty cycle is illustrated in Figure 7g. It is inferred that the heat increases with an increase in pulse duty cycle. The pulse duty ratio with 50% denotes a 50% positive half cycle and a 50% negative half cycle for the 180° conduction mode in which the corresponding load voltage duty ratio is 100%.



(a)

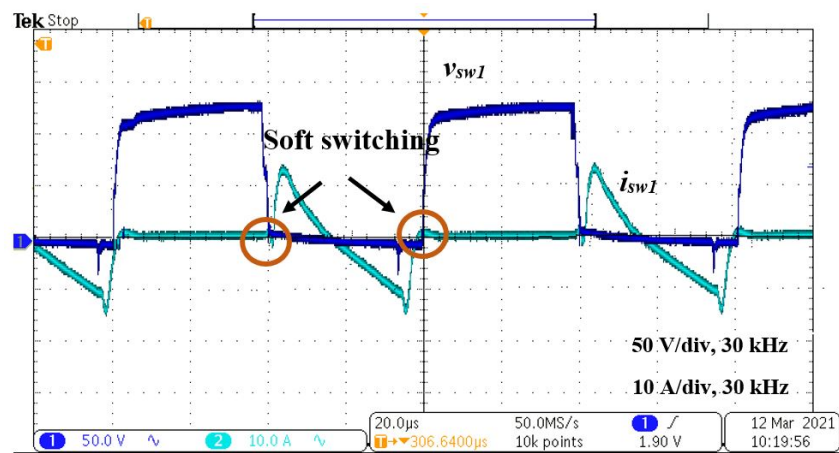


(b)

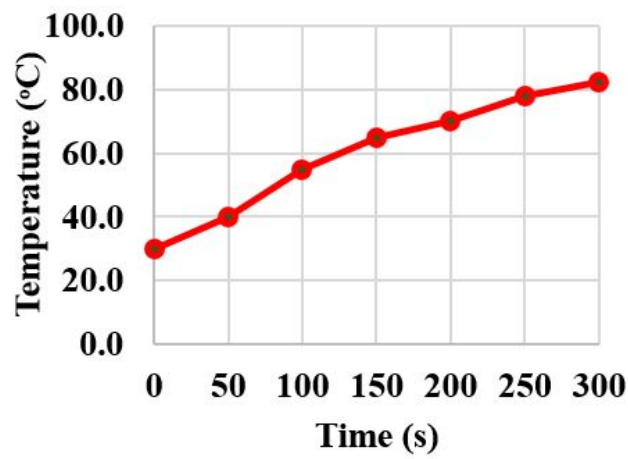


(c)

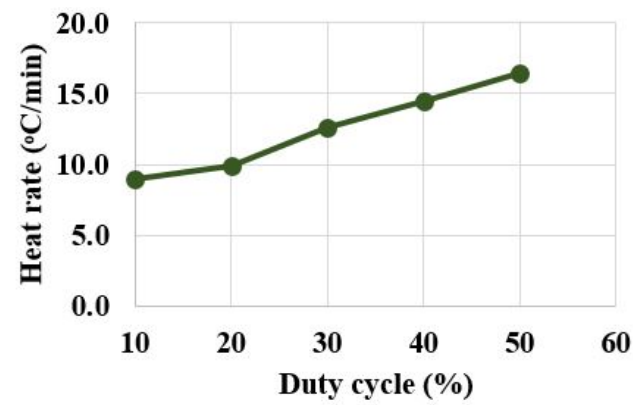
Figure 7. Cont.



(d)



(e)



(f)

Figure 7. Cont.

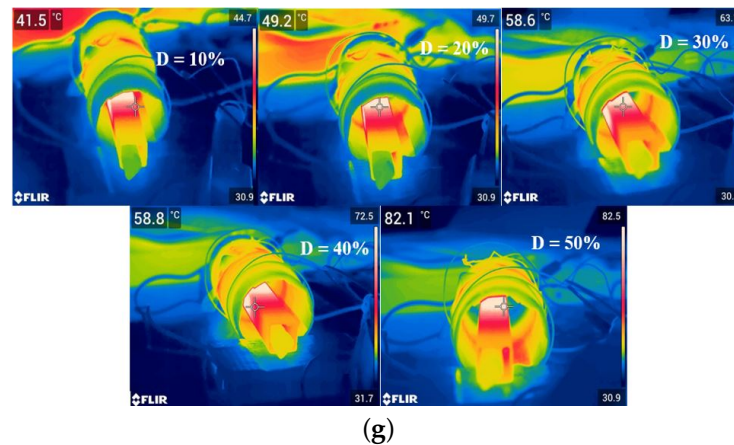


Figure 7. Pulse duty cycle control with 30 kHz frequency. (a) Switching pulses for 50% pulse duty cycle. (b) Output voltage and current waveforms for 50% pulse duty cycle. (c) Output voltage and current waveforms for 10% pulse duty cycle. (d) Switch voltage and current waveforms. (e) Temperature variation. (f) Heat rate for various pulse duty cycles. (g) FLIR thermal image for various pulse duty cycles at $t = 5$ min.

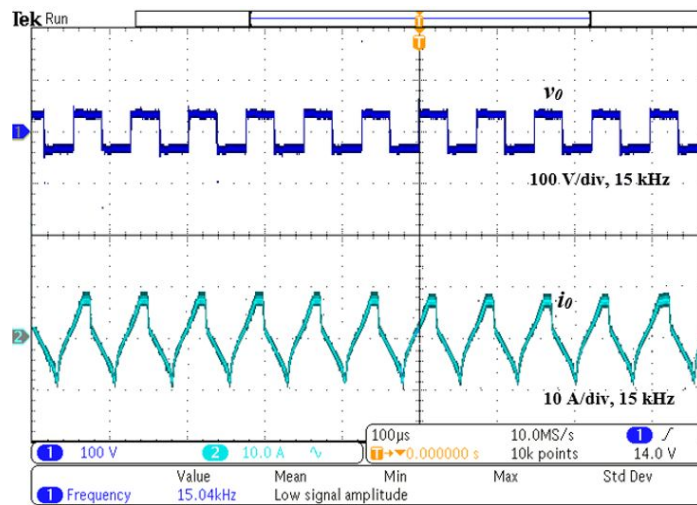
Table 2. Efficiency of pulse duty cycle control.

S. No	Pulse Duty Cycle (%)	Input Voltage (V)	Input Current (A)	Input Power (W)	RMS Value of Output Voltage (V)	RMS Value of Output Current (A)	Output Power (W)	Efficiency (%)
1	10	80	1.79	143	31.59	3.16	99.8	69.8
2	20	80	3.42	273.6	44.7	4.47	199.8	73
3	30	80	4.87	389.6	54.77	5.48	300	77
4	40	80	6.1	488	63.24	6.32	399.9	81.9
5	50	80	6.97	558	70.71	7.07	500	89.6

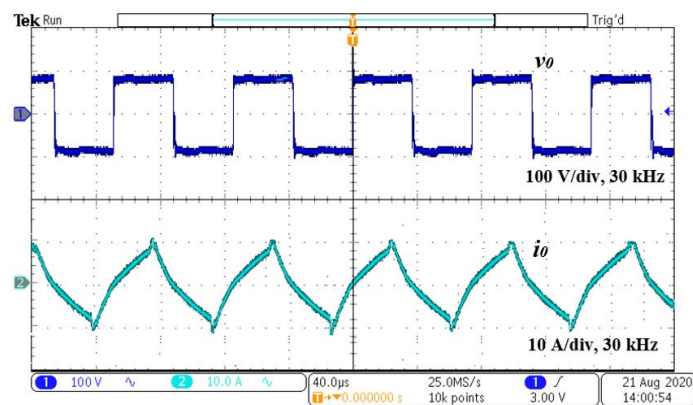
4.2. Variable Frequency Control

The experimental results of variable frequency control are shown in Figure 8. The resonance frequency is 29.5 kHz, and the switching frequency is varied from 13 kHz to 66 kHz to control the output power. The output voltage and the current observed at 15 kHz switching frequency is shown in Figure 8a. The output voltage and current waveforms for 30 kHz and 66 kHz are shown in Figure 8b,c, respectively. For a 66 kHz switching frequency, according to Equation (2), $P_0 = 0.82 \times 500 = 410$ W. The rms value of the current at 66 kHz switching frequency is 6.4 A and P_0 is $6.4^2 \times 10 = 410$ W. The input power (P_{in}) is $80 \times 6.4 = 512$ W. The efficiency for 66 kHz is 80.1%, and it is presented for other switching frequencies in Table 3. It is observed that efficiency is maximum for the resonance condition, and the efficiency is reduced both below and above the resonance frequency due to switching losses. The switch (S_1) voltage and current waveforms for 15 kHz are shown in Figure 8d. It is observed that hard switching is realized as switching frequency is far from the resonance frequency. As the switch is operated in hard switching mode, there exists a ringing effect on the output voltage waveform, which results in more switching loss and stress. Hence, it is advisable to operate the inverter switch in resonant operating mode to reduce switching loss and stress. The temperature variation with respect to time is shown in Figure 8e. The heat rate for various switching frequencies are shown in Figure 8f and FLIR thermal image for various switching frequencies for a fixed time period (5 min) is illustrated in Figure 8g. The temperature varies with respect to the switching frequencies. As the switching frequency is varied, the inverter is operated in hard switching mode, which results in more switching loss. In addition, the frequency ringing effect, heat

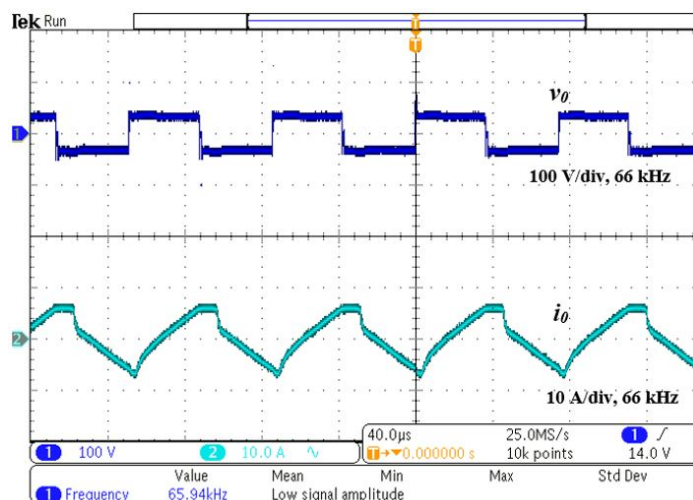
conversion losses, experimental coil design constraints, and capacitor selection restrict the efficiency to 86.9% in real-time implementation.



(a)

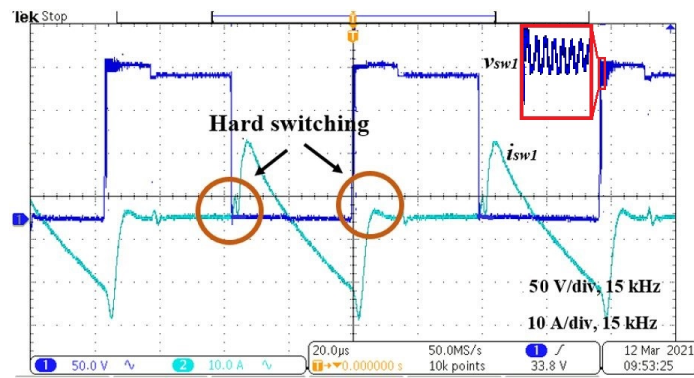


(b)

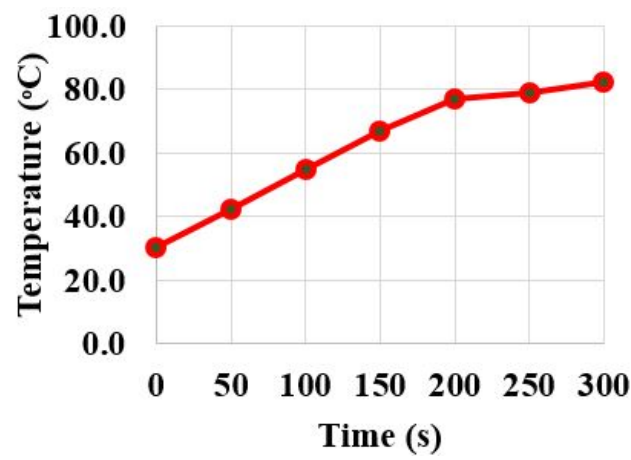


(c)

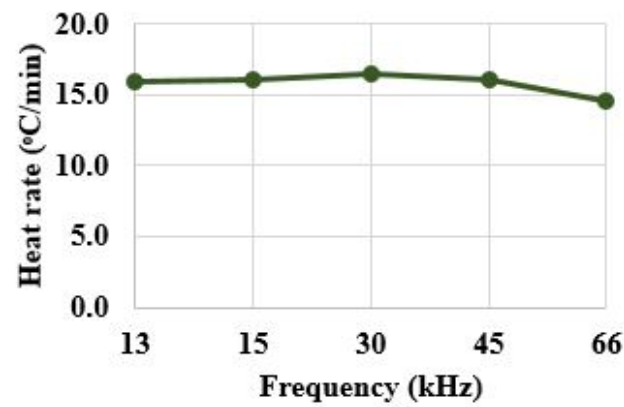
Figure 8. Cont.



(d)

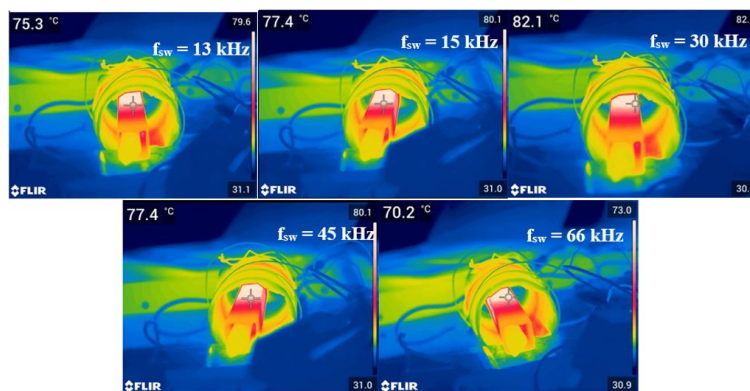


(e)



(f)

Figure 8. Cont.



(g)

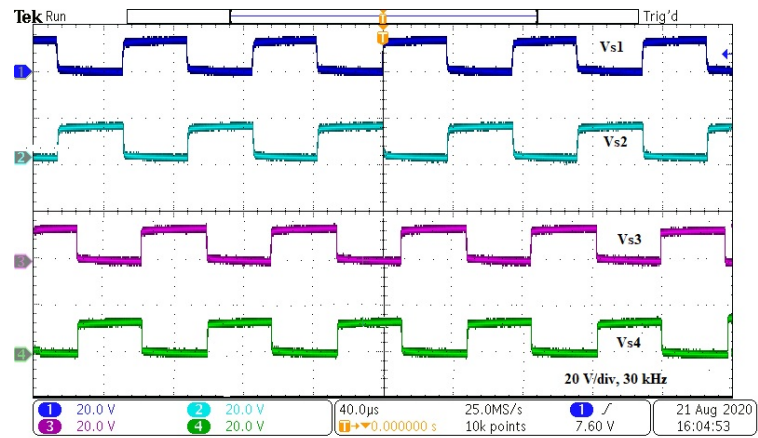
Figure 8. Variable frequency control: output voltage and current waveforms for (a) 15 kHz, (b) 30 kHz, and (c) 66 kHz switching frequency. (d) Switch voltage and current waveforms for 15 kHz switching frequency. (e) Temperature variation. (f) Heat rate for various switching frequencies. (g) FLIR thermal image for various switching frequencies at $t = 5$ min.

Table 3. Efficiency of variable frequency control.

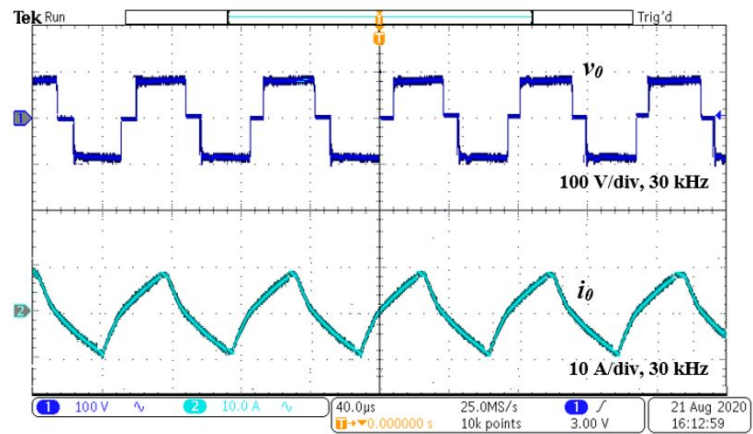
S. No	Switching Frequency (kHz)	Input Voltage (V)	Input Current (A)	Input Power (W)	RMS Value of Output Voltage (V)	RMS Value of Output Current (A)	Output Power (W)	Efficiency (%)
1	13	80	7.29	583	69.21	6.92	479	82.2
2	15	80	7.27	581.6	69.57	6.96	484	83.2
3	30	80	6.97	558	70.71	7.07	500	89.6
4	45	80	7.27	581.6	69.57	6.96	484	83.2
5	66	80	6.4	512	64.03	6.4	410	80.1

4.3. Phase Shift Control

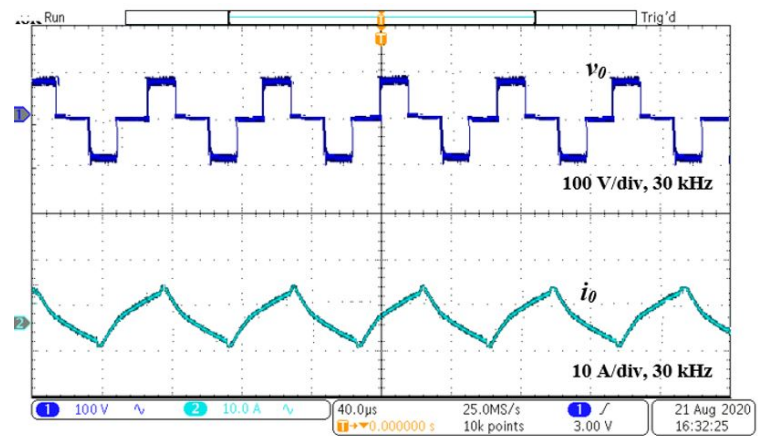
In phase shift control, the switching pulses are shifted with respect to the adjacent leg of the inverter. The variation in rms values of the output voltage and current changes the output power. The experimental results of PSC are shown in Figure 9. The switching pulses, and output voltage and current waveforms for $\phi = 20^\circ$ are shown in Figure 9a,b, respectively. For $\phi = 20^\circ$, according to Equation (5), P_0 is $500 * \cos^2(20/2) = 485$ W. The rms value of the output current is 6.96 A and $P_0 = 6.96^2 * 10 = 484$ W. The input power is $80 * 6.96 = 557$ W. The efficiency for various phase angle is given in Table 4. The output voltage and current waveforms for $\phi = 60^\circ$ is represented in Figure 9c. The soft-switching range for phase shift control is shown in Figure 9d. It is inferred that inverter switches operate in soft switching for ϕ ranging from 0° to 168° . The switch (S_1) voltage and current waveforms for $\phi = 170^\circ$ are shown in Figure 9e, where the switch is operated in hard switching mode. The temperature variation with respect to time is shown in Figure 9f. The heat rate for various phase angles are shown in Figure 9g and FLIR thermal image for various phase angles for a fixed time period (5 min) is illustrated in Figure 9h. As the rms value of output voltage varies, the temperature decreases for an increase in phase angle.



(a)

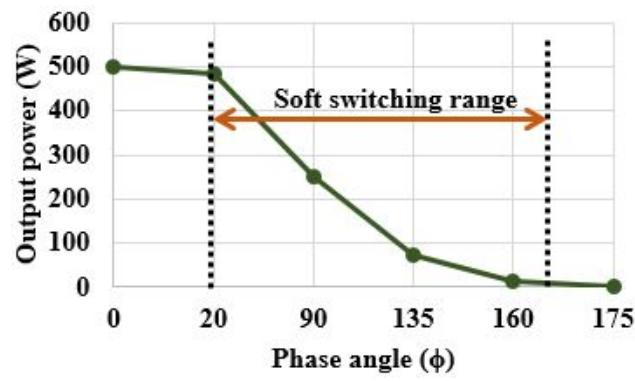


(b)

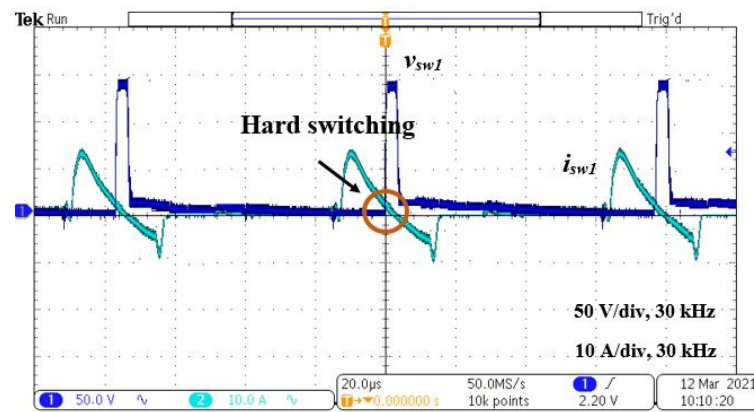


(c)

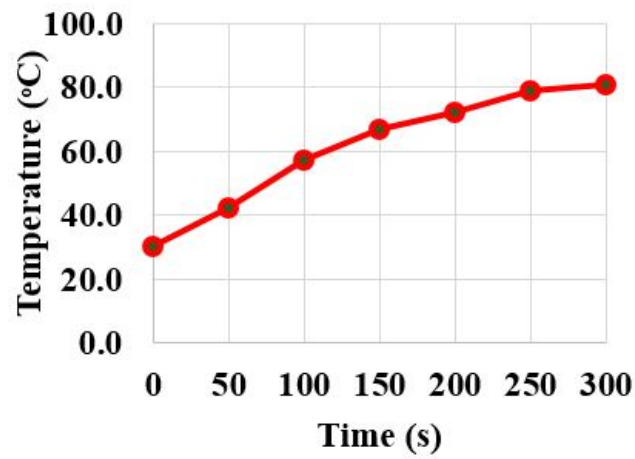
Figure 9. Cont.



(d)

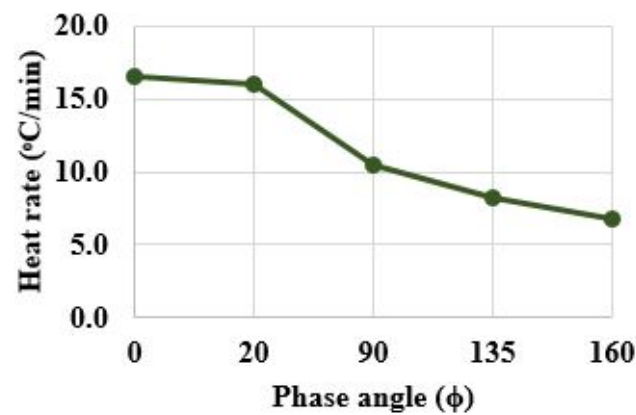


(e)

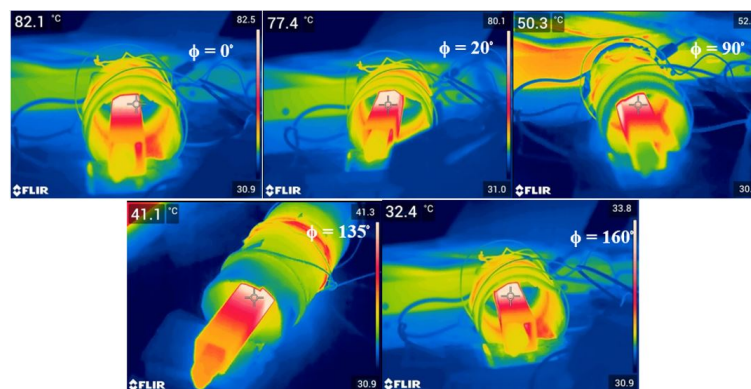


(f)

Figure 9. Cont.



(g)



(h)

Figure 9. Phase shift control. (a) Switching pulses for $\phi = 20^{\circ}$. (b) Output voltage and current waveforms for $\phi = 20^{\circ}$. (c) Output voltage and current waveforms for $\phi = 60^{\circ}$. (d) Soft switching range. (e) Switch voltage and current waveforms for $\phi = 170^{\circ}$. (f) Temperature variation. (g) Heat rate for various phases angles. (h) FLIR thermal image for various phase angles at $t = 5$ min.

Table 4. Efficiency of phase shift control.

S. No	Phase Angle ($^{\circ}$)	Input Voltage (V)	Input Current (A)	Input Power (W)	RMS Value of Output Voltage (V)	RMS Value of Output Current (A)	Output Power (W)	Efficiency (%)
1	0	80	6.97	557.6	70.71	7.07	500	89.6
2	20	80	6.96	557	69.57	6.96	484	87
3	90	80	3.77	301.6	50	5	250	83
4	135	80	1.12	89.6	27.09	2.71	73.4	82
5	160	80	0.23	18.4	12.25	1.22	15	81.5

4.4. Asymmetric Duty Cycle Control

The experimental waveforms corresponding to ADC for 30 kHz switching frequency is shown in Figure 10. The switching pulses and output voltage and current waveforms for $\alpha = 30^{\circ}$ are shown in Figure 10a,b, respectively. For $\alpha = 30^{\circ}$, according to Equation (7), $P_0 = 500 * \cos^2(30/2) = 466.5$ W. The rms value of the output current is 6.8 A and P_0 is $6.8^2 * 10 = 462.4$ W. The input power is $80 * 6.7 = 536$ W. The efficiency for various control angles is given in Table 5. The output voltage and current waveforms for $\alpha = 140^{\circ}$ are shown in Figure 10c. As there is a dead band for zero crossing of current, the switching losses are reduced by making the inverter operate in soft switching mode. The switch (S_1) voltage and current waveforms for $\alpha = 30^{\circ}$ are shown in Figure 10d, where the switch is

operated in soft switching mode. The output voltage is controlled for α ranging from 0° to 165° . The harmonic spectrum for $\alpha = 140^\circ$ is shown in Figure 10e. It is inferred that there exist even harmonics due to the asymmetric voltage waveform. The variation in temperature with respect to time is shown in Figure 10f. The heat rate for various control angles is shown in Figure 10g, and an FLIR thermal image for various phase angles for a fixed time period (5 min) is illustrated in Figure 10h. As the rms value of the output voltage varies, the temperature decreases with an increase in control angle. The ADC technique holds for a rated power operation and variation in the α results in even harmonics in the output voltage due to asymmetric voltage on either half cycle. This results in a reduction in the efficiency.

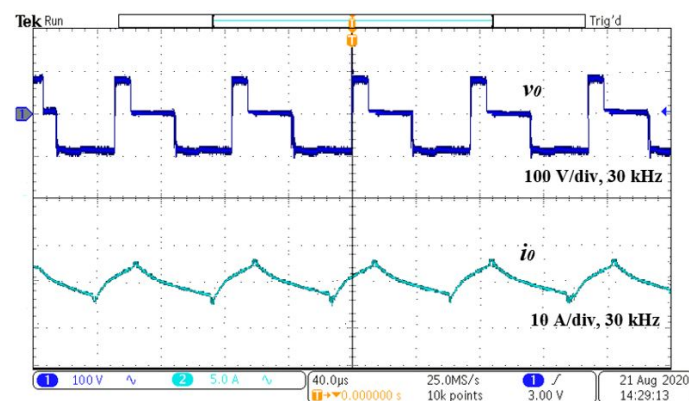
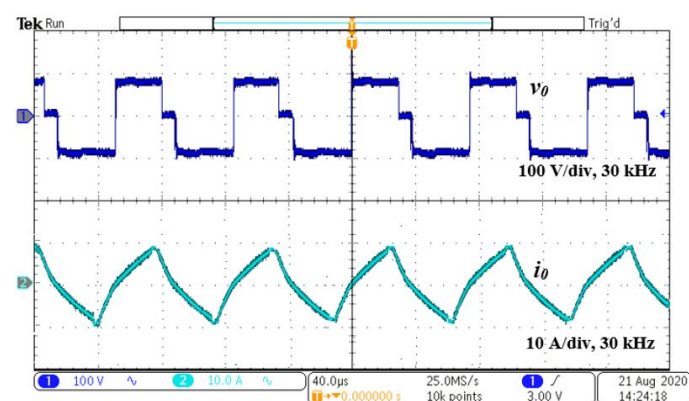
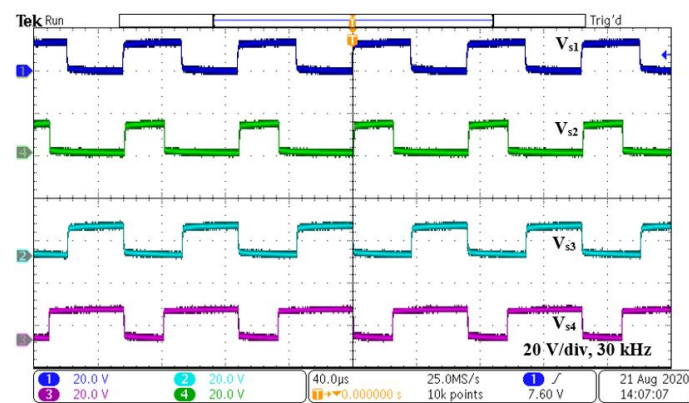


Figure 10. Cont.

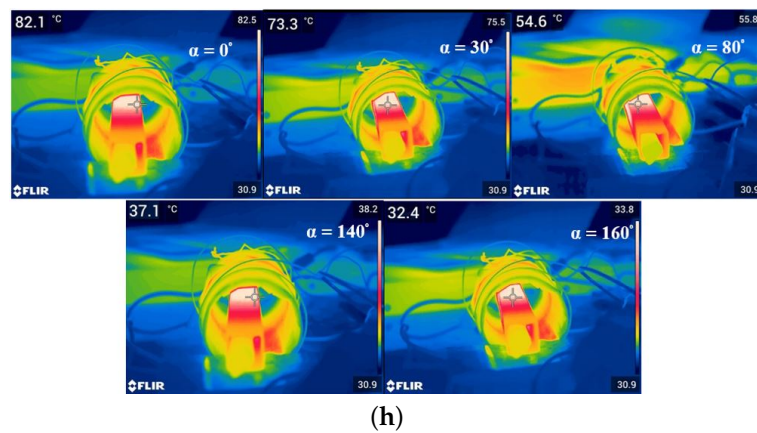
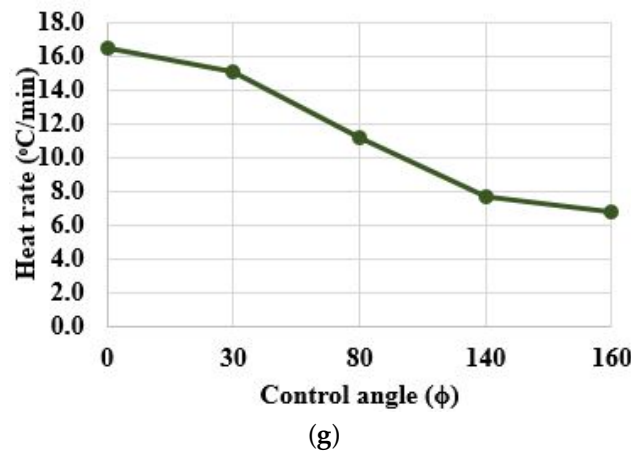


Figure 10. Asymmetrical duty control. (a) Switching pulses for $\alpha = 30^{\circ}$. (b) Output voltage and current waveforms for $\alpha = 30^{\circ}$. (c) Output voltage and current waveforms for $\alpha = 140^{\circ}$. (d) Switch voltage and current waveforms for $\alpha = 30^{\circ}$. (e) Harmonics spectrum for $\alpha = 140^{\circ}$. (f) Temperature variation. (g) Heat rate for various control angles. (h) FLIR thermal image for various control angles at $t = 5$ min.

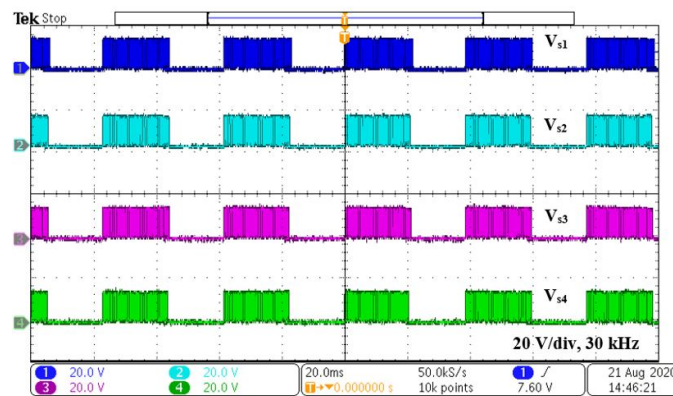
Table 5. Efficiency of asymmetrical duty control.

S. No	Control Angle ($^{\circ}$)	Input Voltage (V)	Input Current (A)	Input Power (W)	RMS Value of Output Voltage (V)	RMS Value of Output Current (A)	Output Power (W)	Efficiency (%)
1	0	80	6.97	557.6	70.71	7.07	500	89.6
2	30	80	6.7	536	68	6.8	462.4	86.2
3	80	80	4.26	341	54.1	5.41	292.6	86
4	140	80	0.87	70	24.2	2.42	58.5	84
5	160	80	0.23	18.4	12.25	1.22	15	81.5

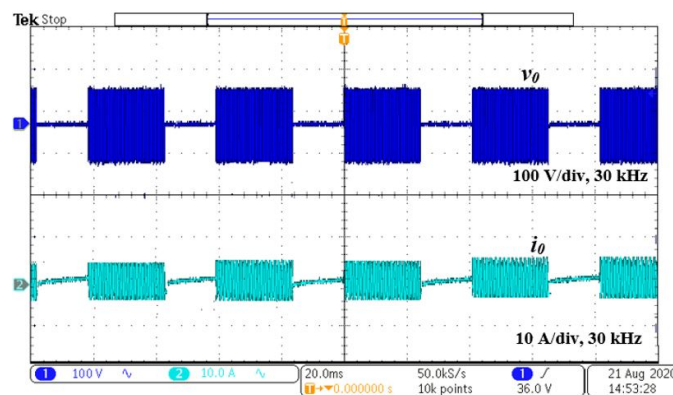
4.5. Pulse Density Modulation Control

One of the most efficient control techniques is the pulse density modulation. In this technique, as the switching frequency and its duty cycle are not varied, the soft-switching operation is retained for the entire power variation. In this technique, a low-frequency signal (20 Hz) is compared with high-frequency switching pulses (30 kHz) to produce the pulse pattern in a manner such that, during the on period of a low-frequency signal, high-frequency pulses are applied to the inverter for powering the load. By controlling the density of high-frequency pulses, the output power is controlled.

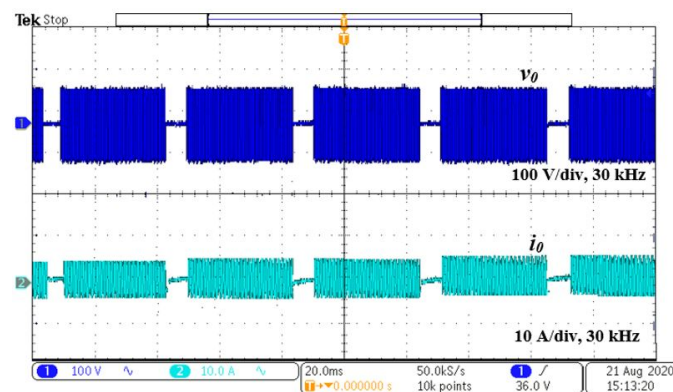
The experimental waveforms for PDM-based control is shown in Figure 11. The switching pulses and output voltage and the current for $D_{PDM} = 60\%$ are shown in Figure 11a,b, respectively. For $60\% D_{PDM}$, according to Equation (9), the calculated $P_0 = 500 \times 0.6 = 300$ W. The rms value of the output current is 5.48 A, and P_0 is $5.48^2 \times 10 = 300$ W. The input power is $80 \times 4.36 = 348.8$ W. The efficiency for various D_{PDM} is given in Table 6. The output voltage and current waveforms for $D_{PDM} = 90\%$ are shown in Figure 11c. As switching frequency is not varied, resonance is maintained for the entire range of operation. The output power is controlled for the D_{PDM} ranging from 0% to 100% . The variation of temperature is shown in Figure 11d. The heat rate for various D_{PDM} is shown in Figure 11e and FLIR thermal image for various D_{PDM} for a fixed time period (5 min) is shown in Figure 11f. The temperature varies with respect to D_{PDM} .



(a)



(b)



(c)

Figure 11. Cont.

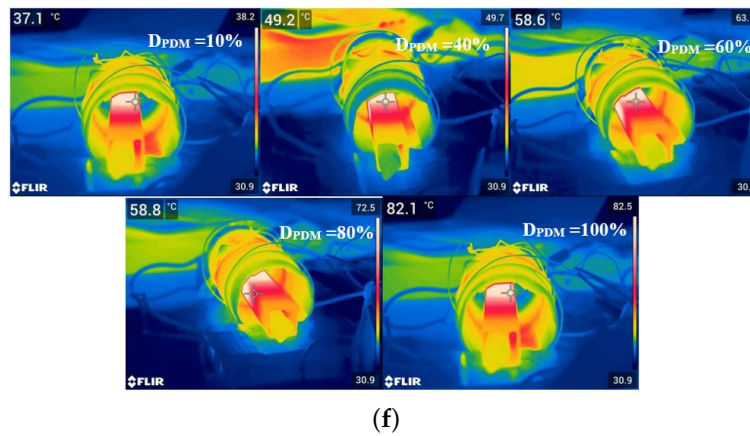
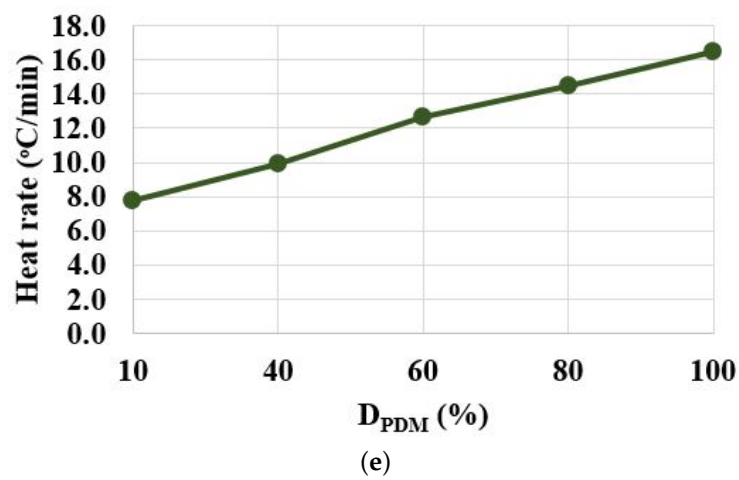
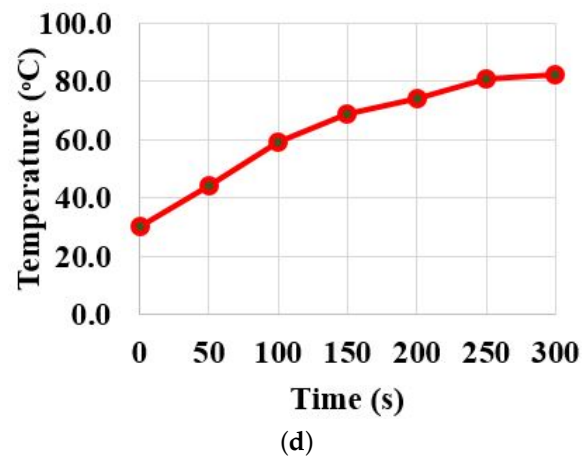


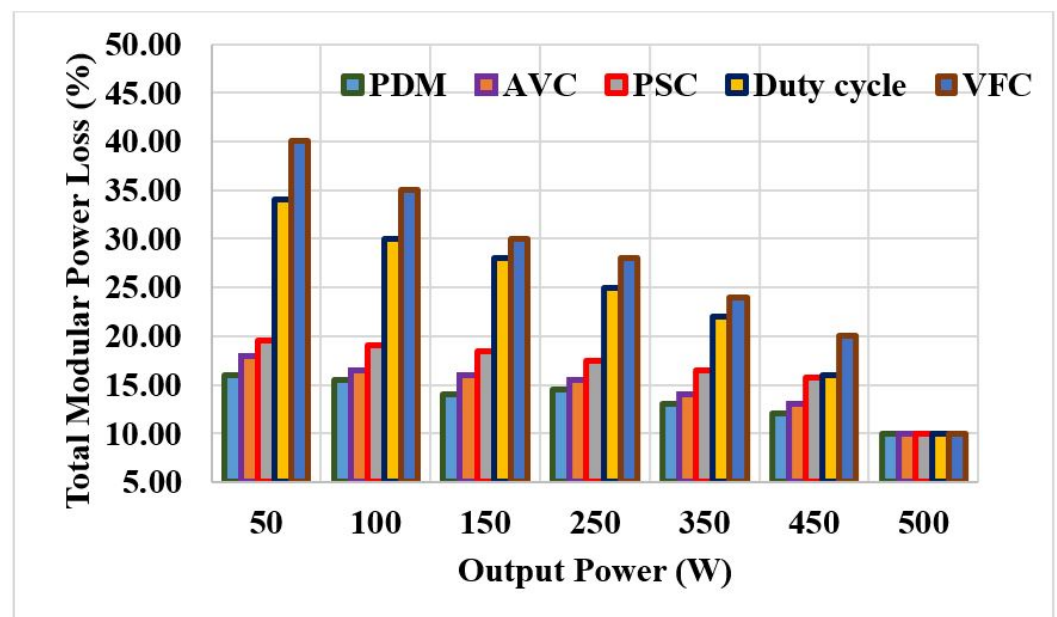
Figure 11. Pulse density modulation control. (a) Switching pulses for $D_{PDM} = 60\%$. (b) Output voltage and current waveforms for $D_{PDM} = 60\%$. (c) output voltage and current waveforms for $D_{PDM} = 90\%$. (d) Temperature variation. (e) Heat rate for various D_{PDM} . (f) FLIR thermal image for various D_{PDM} at $t = 5$ min.

Table 6. Efficiency of pulse density modulation control.

S. No	D_{PDM} (%)	Input Voltage (V)	Input Current (A)	Input Power (W)	RMS Value of Output Voltage (V)	RMS Value of Output Current (A)	Output Power (W)	Efficiency (%)
1	10	80	0.75	60	22.36	2.24	50	83
2	40	80	2.94	235	44.72	4.47	200	85
3	60	80	4.36	339	54.77	5.48	300	86
4	80	80	5.71	457	63.25	6.32	400	87.5
5	100	80	6.97	557.6	70.71	7.07	500	89.6

5. Summary of Discussions on the Experimental Results

In this paper, the various power control techniques used for bifilar coil-based IH systems are discussed. The modular losses are calculated using the formula given in [19]. The modular losses (conduction and switching losses) are calculated to evaluate the best control technique. Figure 12 shows the comparison of total modular power loss with respect to output power. It is inferred that the losses are the same at the rated operating power (500 W) for various control methods. In the PDM control technique, the amount of input power drawn from the supply is at a minimum, which results in a minimum total modular loss as compared with other techniques for the same output power. Similarly, the variation in efficiency with respect to the output power is illustrated in Figure 13. The efficiency of the bifilar coil-based IH system varies between 60% to 89.6% for output power variation. Among the tested control techniques, the PDM control scheme yields higher efficiency (84% to 89.6%) with linear variations in the output power (0% to 100% of rated power).

**Figure 12.** Total modular power loss.

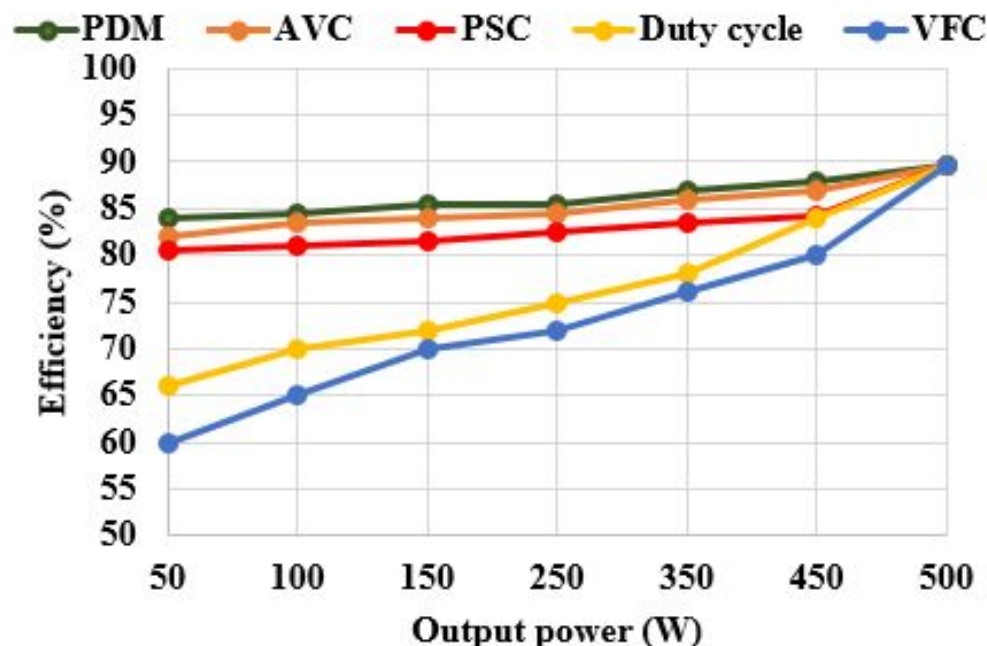


Figure 13. Efficiency of various control techniques.

6. Conclusions

In this work, various control techniques used for IH systems are investigated for bifilar coil-based IH systems used for melting applications. The performance of the system is examined using a full-bridge series-resonant inverter at 500 W output power. The contributions are summarized as follows.

- The pulse density modulation-based control scheme shows optimal performance with respect to heat rate, output variation, and efficiency (maximum of 89.6%). This trend is similar to that of the work published for cooking applications [17,19,31–33].
- Asymmetric duty cycle control can be applied to a system where a wide range of ZVS operations are required. The system possesses even harmonics for various values of α .
- Phase shift control can be deployed for an IH system where power control needs to be varied from 0% to 100% of the rated power. The resonance operation is maintained for ϕ , ranging from 0° to 165° .
- Frequency control is suitable for induction melting applications, since it requires differential heating over the surface and depth of the material.
- A pulse duty cycle-based control scheme is preferred when delivering power for a rated load.

All modulation techniques were implemented using a single PIC 16F877A micro controller, providing a cost effective solution for the prototype developed.

Author Contributions: Conceptualization, A.S., P.V. and R.G.; methodology, P.V.; software, A.S.; validation, P.V., R.G. and S.R.; formal analysis, P.V. and R.G.; investigation, P.V.; resources, B.N.; data curation, S.R.; writing—original draft preparation, P.V.; writing—review and editing, A.S., R.G., S.R. and B.N.; visualization, B.N.; supervision, R.G. and S.R.; project administration, B.N.; funding acquisition, B.N. All authors have read and agreed to the published version of the manuscript.

Funding: This research received no external funding.

Institutional Review Board Statement: Not applicable.

Informed Consent Statement: Not applicable.

Data Availability Statement: Not applicable.

Conflicts of Interest: The authors declare no conflict of interest.

References

1. Vishnuram, P.; Ramachandran, G.; Ramasamy, S.; Dayalan, S. A comprehensive overview of power converter topologies for induction heating applications. *Int. Trans. Electr. Energy Syst.* **2020**, *30*, e12554. [\[CrossRef\]](#)
2. Lozinskii, M.G. *Industrial Applications of Induction Heating*; Pergamon: Oxford, UK, 1969.
3. Moreland, W.C. The Induction Range: Its Performance and Its Development Problems. *IEEE Trans. Ind. Appl.* **1973**, *IA-9*, 81–85. [\[CrossRef\]](#)
4. Acero, J.; Burdio, J.M.; Barragan, L.A.; Navarro, D.; Alonso, R.; Garcia, J.R.; Monterde, F.; Hernandez, P.; Llorente, S.; Garde, I. The domestic induction heating appliance: An overview of recent research. In Proceedings of the 2008 Twenty-Third Annual IEEE Applied Power Electronics Conference and Exposition, Austin, TX, USA, 24–28 February 2008; pp. 651–657. [\[CrossRef\]](#)
5. Lucía, O.; Maussion, P.; Dede, E.J.; Burdío, J.M. Induction Heating Technology and Its Applications: Past Developments, Current Technology, and Future Challenges. *IEEE Trans. Ind. Electron.* **2014**, *61*, 2509–2520. [\[CrossRef\]](#)
6. Fujita, H.; Uchida, N.; Ozaki, K. A New Zone-Control Induction Heating System Using Multiple Inverter Units Applicable Under Mutual Magnetic Coupling Conditions. *IEEE Trans. Power Electron.* **2011**, *26*, 2009–2017. [\[CrossRef\]](#)
7. Fernández, O.; Delgado, J.; Martínez, F.; Correa, J.; Heras, M. Design and implementation of a 120A resonant inverter for induction furnace. In Proceedings of the 2013 IEEE International Autumn Meeting on Power Electronics and Computing (ROPEC), Morelia, Mexico, 13–15 November 2013; pp. 1–6. [\[CrossRef\]](#)
8. Yongyuth, N.; Viriya, P.; Matsuse, K. Analysis of a Full-Bridge Inverter for Induction Heating Using Asymmetrical Phase-Shift Control under ZVS and NON-ZVS Operation. In Proceedings of the 7th International Conference on Power Electronics and Drive Systems, Bangkok, Thailand, 27–30 November 2007; pp. 476–482. [\[CrossRef\]](#)
9. Villa, J.; Navarro, D.; Dominguez, A.; Artigas, J.I.; Barragan, L.A. Vessel Recognition in Induction Heating Appliances—A Deep-Learning Approach. *IEEE Access* **2021**, *9*, 16053–16061. [\[CrossRef\]](#)
10. Shenkman, A.; Axelrod, B.; Berkovich, Y. Single-switch AC-AC converter with high power factor and soft commutation for induction heating applications. *IEEE Proc. Electr. Power Appl.* **2001**, *148*, 469–474. [\[CrossRef\]](#)
11. Sarnago, H.; Lucía, O.; Mediano, A.; Burdío, J.M. Class-D/DE Dual-Mode-Operation Resonant Converter for Improved-Efficiency Domestic Induction Heating System. *IEEE Trans. Power Electron.* **2013**, *28*, 1274–1285. [\[CrossRef\]](#)
12. Ahmed, N.; Nakaoka, M. Boost-half-bridge edge resonant soft switching PWM high-frequency inverter for consumer induction heating appliances. *IEEE Proc. Electr. Power Appl.* **2006**, *153*, 932–938. [\[CrossRef\]](#)
13. Forest, F.; Faucher, S.; Gaspard, J.; Montloup, D.; Huselstein, J.; Joubert, C. Frequency-Synchronized Resonant Converters for the Supply of Multiwinding Coils in Induction Cooking Appliances. *IEEE Trans. Ind. Electron.* **2007**, *54*, 441–452. [\[CrossRef\]](#)
14. Lucia, O.; Burdio, J.M.; Millan, I.; Acero, J.; Puyal, D. Load-Adaptive Control Algorithm of Half-Bridge Series Resonant Inverter for Domestic Induction Heating. *IEEE Trans. Ind. Electron.* **2009**, *56*, 3106–3116. [\[CrossRef\]](#)
15. Lucía, O.; Burdío, J.M.; Barragán, L.A.; Acero, J.; Millán, I. Series-Resonant Multiinverter for Multiple Induction Heaters. *IEEE Trans. Power Electron.* **2010**, *25*, 2860–2868. [\[CrossRef\]](#)
16. Sarnago, H.; Lucía, O.; Burdio, J.M. A Versatile Resonant Tank Identification Methodology for Induction Heating Systems. *IEEE Trans. Power Electron.* **2018**, *33*, 1897–1901. [\[CrossRef\]](#)
17. Meziane, B.; Zeroug, H. Comprehensive Power Control Performance Investigations of Resonant Inverter for Induction Metal Surface Hardening. *IEEE Trans. Ind. Electron.* **2016**, *63*, 6086–6096. [\[CrossRef\]](#)
18. Bi, C.; Lu, H.; Jia, K.; Hu, J.; Li, H. A Novel Multiple-Frequency Resonant Inverter for Induction Heating Applications. *IEEE Trans. Power Electron.* **2016**, *31*, 8162–8171. [\[CrossRef\]](#)
19. Vishnuram, P.; Ramachandran, G.; Ramasamy, S. A Novel Power Control Technique for Series Resonant Inverter-Fed Induction Heating System with Fuzzy-Aided Digital Pulse Density Modulation Scheme. *Int. J. Fuzzy Syst.* **2017**, *20*. [\[CrossRef\]](#)
20. Acero, J.; Carretero, C.; Alonso, R.; Burdio, J.M. Quantitative Evaluation of Induction Efficiency in Domestic Induction Heating Applications. *IEEE Trans. Magn.* **2013**, *49*, 1382–1389. [\[CrossRef\]](#)
21. Wang, C.S.; Stielau, O.; Covic, G. Design considerations for a contactless electric vehicle battery charger. *IEEE Trans. Ind. Electron.* **2005**, *52*, 1308–1314. [\[CrossRef\]](#)
22. Chudnovsky, V.; Axelrod, B.; Shenkman, A.L. An approximate analysis of a starting process of a current source parallel inverter with a high-Q induction heating load. *IEEE Trans. Power Electron.* **1997**, *12*, 294–301. [\[CrossRef\]](#)
23. de Miranda, C.M.; Pichorim, S.F. A Self-Resonant Two-Coil Wireless Power Transfer System Using Open Bifilar Coils. *IEEE Trans. Circuits Syst. II Express Briefs* **2017**, *64*, 615–619. [\[CrossRef\]](#)
24. Miranda, C.; Pichorim, S. On the self-resonant frequency reduction of closed- and open-bifilar coils. *Int. J. Circuit Theory Appl.* **2019**, *47*, 641–653. [\[CrossRef\]](#)
25. Vishnuram, P.; Ramachandran, G. Capacitor-less induction heating system with self-resonant bifilar coil. *Int. J. Circuit Theory Appl.* **2020**, *48*, 1411–1425. [\[CrossRef\]](#)
26. Sarnago, H.; Lucia, O.; Mediano, A.; Burdio, J. High-efficiency parallel quasi-resonant current source inverter featuring SiC metal-oxide semiconductor field-effect transistors for induction heating systems with coupled inductors. *IET Power Electron.* **2013**, *6*, 183–191. [\[CrossRef\]](#)
27. Bojoi, R.; Griva, G.; Profumo, F.; Cesano, M.; Natale, L. Shunt active power filter implementation for induction heating applications. In Proceedings of the Twentieth Annual IEEE Applied Power Electronics Conference and Exposition, Austin, TX, USA, 6–10 March 2005; Volume 3, pp. 1674–1679. [\[CrossRef\]](#)

28. Barragan, L.; Burdio, J.; Artigas, J.; Navarro, D.; Acero, J.; Puyal, D. Efficiency optimization in ZVS series resonant inverters with asymmetrical voltage-cancellation control. *IEEE Trans. Power Electron.* **2005**, *20*, 1036–1044. [[CrossRef](#)]
29. Burdio, J.; Barragan, L.; Monterde, F.; Navarro, D.; Acero, J. Asymmetrical voltage-cancellation control for full-bridge series resonant inverters. *IEEE Trans. Power Electron.* **2004**, *19*, 461–469. [[CrossRef](#)]
30. Ahmed, N.A. High-Frequency Soft-Switching AC Conversion Circuit With Dual-Mode PWM/PDM Control Strategy for High-Power IH Applications. *IEEE Trans. Ind. Electron.* **2011**, *58*, 1440–1448. [[CrossRef](#)]
31. Vishnuram, P.; Ramachandran, G. A simple multi-frequency multiload independent power control using pulse density modulation scheme for cooking applications. *Int. Trans. Electr. Energy Syst.* **2021**, *31*, e12771. [[CrossRef](#)]
32. Vishnuram, P.; Ramachandran, G.; Thanikanti, S.B.; Nastasi, B. Induction Heating in Domestic Cooking and Industrial Melting Applications: A Systematic Review on Modelling, Converter Topologies and Control Schemes. *Energies* **2021**, *14*, 6634. [[CrossRef](#)]
33. Vishnuram, P.; Dayalan, S.; Thanikanti, S.B.; Balasubramanian, K.; Nastasi, B. Single Source Multi-Frequency AC-AC Converter for Induction Cooking Applications. *Energies* **2021**, *14*, 4799. [[CrossRef](#)]